New Insights into Variations in Enceladus Plume Particle Launch Velocities from Cassini-VIMS Spectral Data

H. Sharma[1] , M. M. Hedman[1] , and S. Vahidinia[2]
[1] University of Idaho, 875 Perimeter Drive, Moscow, ID 83844, USA; hbbhardwaj02@gmail.com
[2] NASA Ames Research Center, Mountain View, CA 94035, USA

Abstract

Enceladus's plume consists mainly of a mixture of water vapor and solid ice particles that may originate from a subsurface ocean. The physical processes underlying Enceladus's plume particle dynamics are still being debated, and quantifying the particles' size distribution and launch velocities can help constrain these processes. Cassini's Visual and Infrared Mapping Spectrometer observed the Enceladus plume over a wavelength range of 0.9–5.0 μm for a significant fraction of Enceladus's orbital period on three dates in the summer of 2017. We find that the relative brightness of the plume on these different dates varies with wavelength, implying that the particle size distribution in the plume changes over time. These observations also enable us to study how the particles' launch velocities vary with time and observed wavelength. We find that the typical launch velocity of particles remains between 140 and 148 m s^{-1} at wavelengths between 1.2 and 3.7 μm. This may not be consistent with prior models where particles are only accelerated by interactions with the vent walls and gas and could imply that mutual particle collisions close to the vent are more important than previously recognized.

Unified Astronomy Thesaurus concepts: Enceladus (2280); Dust physics (2229); Volcanism (2174); Infrared spectroscopy (2285)

1. Introduction

Enceladus emits a plume of water vapor and icy particles from a series of fissures located near its south pole (Dougherty et al. 2006; Porco et al. 2006; Spencer et al. 2006). This plume can shed light on the processes operating inside Enceladus and the driving forces behind this geological activity. Measurements from several instruments on board the Cassini spacecraft have been utilized to examine the plume's characteristics (Hansen et al. 2006; Spahn et al. 2006; Waite et al. 2006, 2009; Hedman et al. 2009; Postberg et al. 2009; Schenk et al. 2018). At the same time, several different theoretical models have been developed to explain various aspects of the plume (Kieffer et al. 2006; Hurford et al. 2007; Brilliantov et al. 2008; Schmidt et al. 2008; Ingersoll & Pankine 2010; Kite & Rubin 2016; Goldstein et al. 2018; Ermakov et al. 2021).

One important source of information about the physics behind Enceladus's plume are its variations over time periods ranging from days to years. Variations have been observed in the plume's total particle output by both the Visual and Infrared Mapping Spectrometer (VIMS) instrument (Hedman et al. 2013) and the Imaging Science Subsystem (ISS) cameras (Nimmo et al. 2014; Porco et al. 2014; Helfenstein & Porco 2015; Ingersoll & Ewald 2017; Ingersoll et al. 2020) on board the Cassini spacecraft. Most dramatically, both the ISS and VIMS data show that the plume's ice grain output varies systematically with the moon's orbital phase (the angular distance between the moon's current position and its orbital pericenter, equivalent to the moon's orbital mean anomaly). The primary maximum in the plume's brightness occurs close to orbital apocenter (orbital phase of 180°), where the particle

output is roughly four times higher than it is at other points in its orbit. The most likely cause of the variations on orbital timescales are the tidal stresses experienced by Enceladus as it moves in its eccentric orbit around Saturn (Hurford et al. 2007, 2012; Nimmo et al. 2007; Smith-Konter & Pappalardo 2008; Goldstein et al. 2018). Variations in the plume's activity on longer timescales were also seen by both VIMS (Hedman et al. 2013) and ISS (Ingersoll & Ewald 2017; Porco et al. 2018; Ingersoll et al. 2020), which may be due to either a 5% decrease in the eccentricity of the orbit as part of a ∼11 yr tidal cycle or slow (and perhaps seasonal) changes in the clogging of vents (Ingersoll & Ewald 2017; Porco et al. 2018). The plume is also prone to stochastic time variability on month-to-year timescales (Ingersoll et al. 2020), whose origins are still unclear and may be due to individual jets turning on and off (Spitale & Porco 2007; Ingersoll & Pankine 2010; Hurford et al. 2012; Nimmo et al. 2014; Porco et al. 2014; Nakajima & Ingersoll 2016; Teolis et al. 2017).

Compared to the relatively dramatic brightness variations listed above, trends in other plume particle properties like launch velocity and size distributions are subtler. Hedman et al. (2009) found some differences in the spectral properties of the plume among the early VIMS observations, but these were of marginal statistical significance. Both Hedman et al. (2013) and Ingersoll & Ewald (2017) found small variations in the launch velocity with orbital phase. Nimmo et al. (2014) also reported an essentially constant scale height parameter for the plume. These observations are generally consistent with models where increasing crack width increases the total mass flow but has little effect on particle velocities (Ingersoll & Pankine 2010).

This paper aims to quantify variations in the plume's properties using spectral data obtained by the VIMS on board the Cassini spacecraft (Brown et al. 2004). VIMS can provide new information about trends in the particle size and velocity distribution over time because it was able to observe the plume over a broad range of near-infrared wavelengths. More
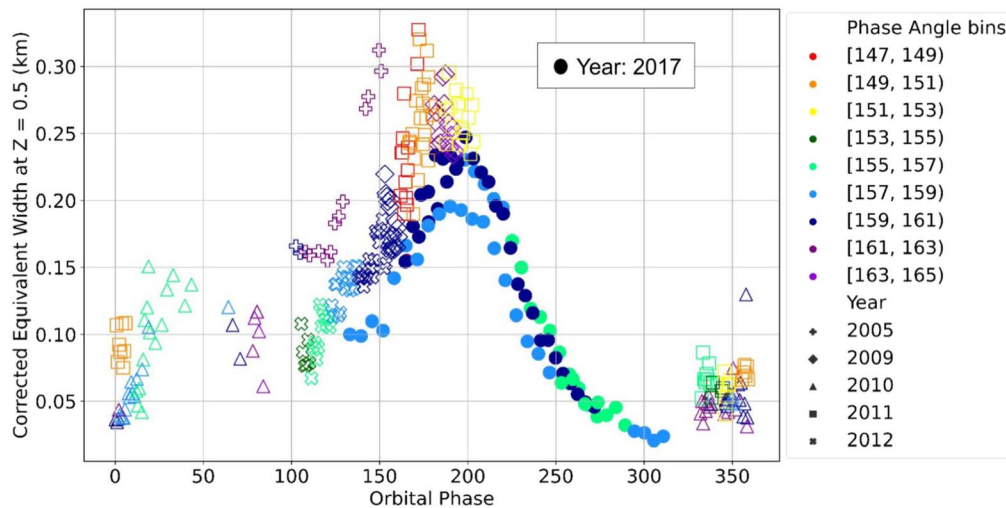
Figure 1. Overview of variations in the plume's brightness (expressed in terms of the corrected equivalent width at a wavelength of 0.88–1.56 μm and an altitude of 85 km; see text for details) as a function of orbital phase. This figure compares the plume brightness estimates derived in this study (shown as filled circles) with previously published estimates from earlier in the Cassini mission (shown as open symbols; Hedman et al. 2013). Note that the corrected equivalent width used in this particular plot includes the phase-angle correction described in Hedman et al. (2013) in order to facilitate comparisons among the different data sets.

specifically, we will examine VIMS data obtained on three dates: 2017 June 18, August 2, and August 28. There is a clear maximum in the plume's brightness around apoapsis in the VIMS data on all three of these dates (see Figure 1), consistent with previous ISS results (Ingersoll et al. 2020). The VIMS observations at short wavelengths also show the same variations in the plume's brightness among the three orbits, where the brightness increases from June 18 to August 2 and decreases again on August 28 as reported by Ingersoll et al. (2020). However, the VIMS data show that these variations in plume brightness across the three different orbits being studied here are not the same at all wavelengths, suggesting that the plume's particle size distribution also varied over this time period of 3 months. In addition, we find that the launch velocities of the plume particles do not vary as much with wavelength as published models would predict (Schmidt et al. 2008; Degruyter & Manga 2011, but see Schmidt (2014) for modified models that may be consistent with these observations).

Our methods for extracting information about the plume from the VIMS data are described in Section 2. This analysis begins by converting the raw VIMS data to estimates of the plume's spectra at various distances from the south pole. These spectra are then converted into constraints on the plume's overall intensity and the particles' typical launch velocity assuming that the particles follow ballistic trajectories. The results of these calculations are presented in Section 3. Finally, in Section 4 we further discuss the implication of the observed spectral trends in the brightness and typical launch velocity of particles. Note that this paper is focused on documenting the spectral trends in these data. Detailed spectral modeling of these trends will be the subject of future work.

2. Methods

This section describes the steps by which the relevant VIMS data are reduced into standardized estimates of the plume brightness and typical launch velocity at a range of wavelengths. Section 2.1 describes the geometry and calibration of the VIMS observations for the three dates in 2017 being studied here. Section 2.2 details how these data are processed

to obtain high signal-to-noise ratio spectra of the plume at different altitudes. Finally, Section 2.3 shows how these data are fit to obtain the brightness and typical launch velocity at different wavelengths.

2.1. Data

VIMS was an imaging spectrometer on board the Cassini spacecraft that covered the 0.3–5.1 μm wavelength range using 352 spectral channels. This instrument could view an array of up to 64×64 locations in the sky to produce a spectral–spatial image "cube" (Brown et al. 2004). In this paper, we focus exclusively on the infrared spectra obtained by the VIMS-IR channel that measured the brightness in 256 wavelength bands between 0.88 and 5.1 μm with a typical spectral resolution of 0.016 μm. Further, we have removed the data corresponding to spectral channels at 1.23 μm (channel 118) and at 4.75 μm (channel 330), as they contain null values owing to being hot pixels on the detector (Clark et al. 2018) and exclude data beyond 4.0 μm because the signal-to-noise ratio is significantly lower at these wavelengths. This reduces the number of spectral channels considered here from 256 to 186.

This investigation examines VIMS observations of Enceladus from three different Cassini orbits (designated 279, 286, and 290) corresponding to the following 3 days: 2017 June 18, August 2, and August 28. During all three of these days, VIMS viewed Enceladus from similarly high phase angles (156°–162°) over a similar range of the moon's orbital phase. The parameters for these three observations are listed in Table 1. Note that all three observations cover orbital phases around 180°, when the plume is most active, and are at high enough phase angles for the plume signals to be clearly detectable.

The raw data in each cube are converted into I/F values (a standard measure of reflectance) using standard calibration routines (the specific calibration being RC19; Clark et al. 2018). To facilitate comparisons among the observations, the observation geometry for each cube is computed using the appropriate SPICE kernels, and the brightness data are reprojected onto a regular array of Cartesian coordinates [x, y] containing the moon's spin axis. In these coordinates the center of Enceladus is located at [0, 0] and the negative y-axis
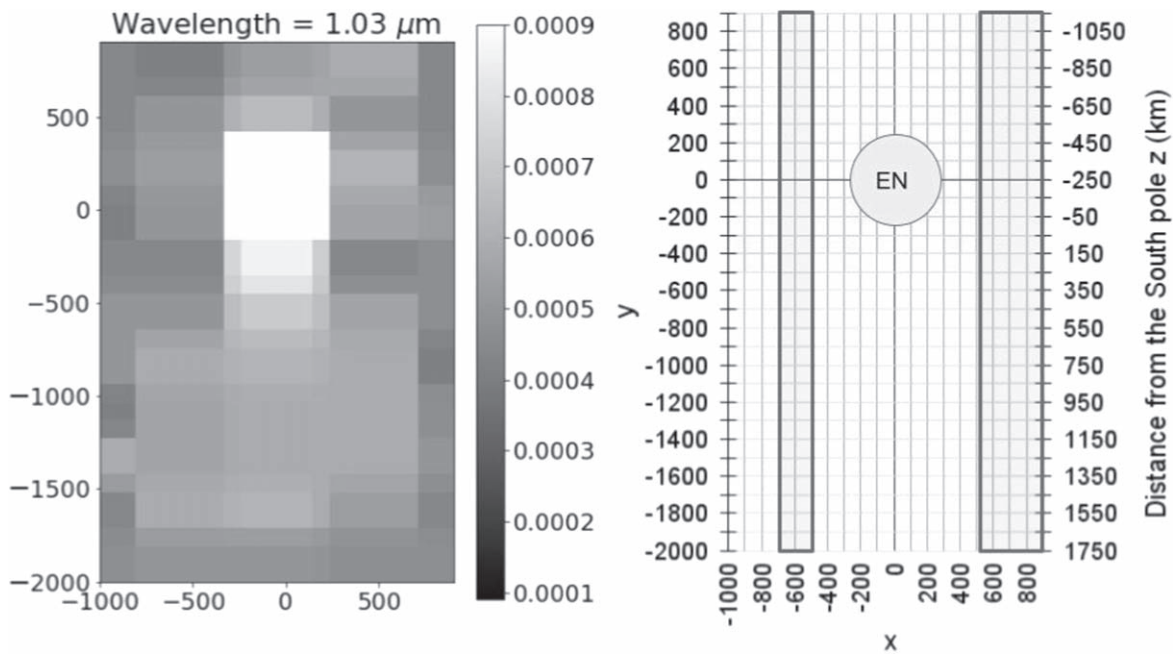
Figure 2. The spatial geometry of the reprojected VIMS cubes. On the left is a sample image of Enceladus and its plume at a wavelength of 1.03 μm derived from a single reprojected cube (CM_1876456410_1) obtained at an orbital phase of 200° during Orbit no. 279 on June 18. On the right is the geometry of the reprojected VIMS cubes. The reprojected data plane is defined using Cartesian coordinates [x, y], with Enceladus at the center at [0, 0], and the negative y-axis is aligned with the moon's spin axis. The left vertical axis and the horizontal axis show the [x, y] coordinates for the cube. For the right vertical axis of the figure the y coordinate has been converted into altitude above Enceladus's south pole ($z = -(250 + y)$ in km). The outlined regions on either side correspond to the region used to calculate background signal levels.

Table 1
The Three Data Sets Studied in This Paper

Orbit No./Date	Orbital Phase[c]	Phase Angle[d]	Range[a] (km)	Longitude[b]	Cubes	No. of Cubes Before Binning	No. of Cubes After Binning
279/2017 Jun 18	162°–319°	156°–161°	837,300–1,093,300	11°–164°	CM_1876443559_1–CM_1876495215_1	302	28
286/2017 Aug 2	162°–286°	159°–161°	822,700–1,063,000	29°–150°	CM_1880355368_1–CM_1880396071_6	293	26
290/2017 Aug 28	130°–281°	156°–158°	868,600–1,140,800	13°–160°	CM_1882597042_1–CM_1882646878_5	240	23

Notes.
[a] Range defines the distance between Enceladus and Cassini.
[b] Subspacecraft longitude on Enceladus.
[c] The orbital phase refers to the position of Enceladus in its orbit around Saturn, also known as mean anomaly.
[d] The phase angle is the angle formed between the Sun, the target being imaged (Enceladus and its plume), and the spacecraft (Cassini). Note that this number does not increase continuously over the course of the observation but stays in the given range.

is aligned with Enceladus's spin axis. In the resulting maps x ranges from -1000 to 900 km and y ranges from -2000 to 900 km. Both coordinates are sampled every 100 km. Figure 2 shows the extent of the coordinates x and y. We also use the y coordinate to compute the distance from Enceladus's south pole (i.e., the plume's altitude) as $z = -(250 + y)$ in km.

### 2.2. Extracting Brightness Spectra at Different Altitudes and Times

The first step in extracting plume spectra from these cubes is to remove cubes that had instrumental artifacts that made their spectra discrepant from the rest of the observation. We identified these anomalous cubes by first averaging the brightness in the region of Enceladus's plume at each wavelength over all values of x from -400 to 400 km and

all values of y between -300 km and beyond. A median filter is then applied to this list of average brightness values at each wavelength. Any image/cube that lies outside the 3σ range of the median brightness was flagged as an outlier for that spectral channel. We then compared the outlier list of each spectral channel, and if a cube appeared as an outlier for over 35 spectral channels, it was regarded as unreliable and so removed from further consideration. This procedure led to the removal of 22 cubes from the data on June 18/Orbit no. 279, 24 cubes from the data on August 2/Orbit no. 286, and 11 cubes from the data on August 28/Orbit no. 290 (see the Appendix for an explicit list of these cubes).

After removing the outliers and before applying background removal techniques, the cubes are coadded. Spectra derived from the individual remaining cubes had low signal-to-noise ratio, so we averaged together sets of 10 cubes to improve the
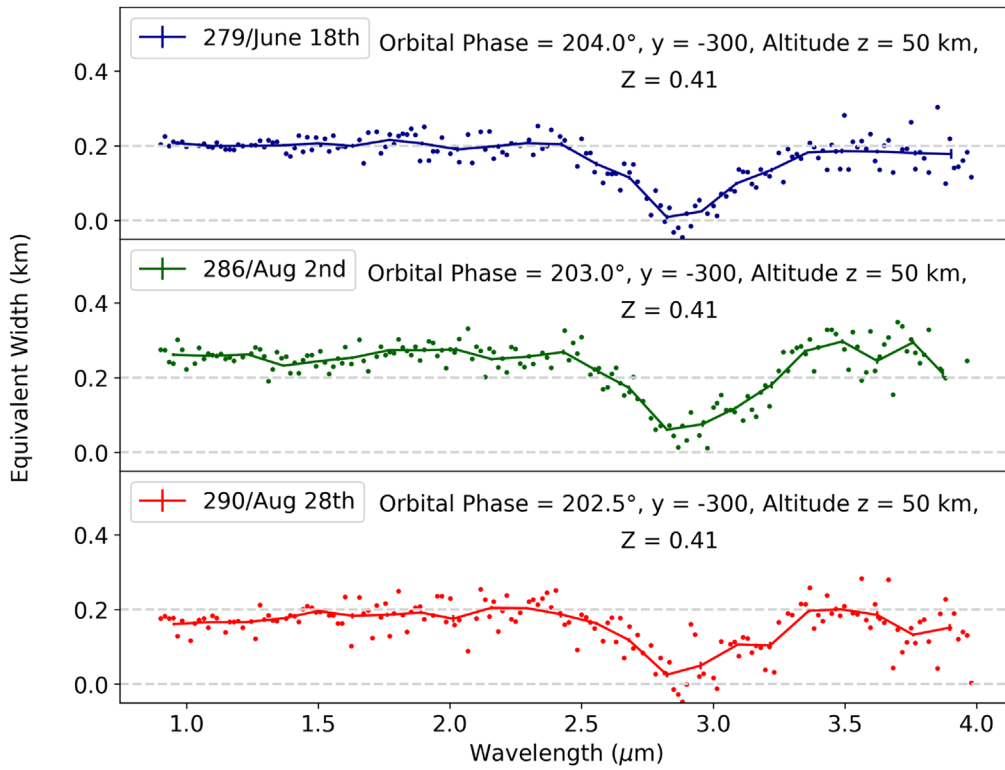
Figure 3. Example Enceladus plume spectra, showing the plume's equivalent width (in km; see Section 2.2) vs. wavelength (in μm) at similar orbital phases for all three orbits. An orbital phase close to 200° is chosen, as the signal is strongest closer to the plume maxima at apoapsis. The points show the equivalent widths for individual spectral channels (after removing outliers before 2.5 μm and after 3.3 μm), and the line plot with error bars shows the data after averaging each spectrum over eight wavelength channels.
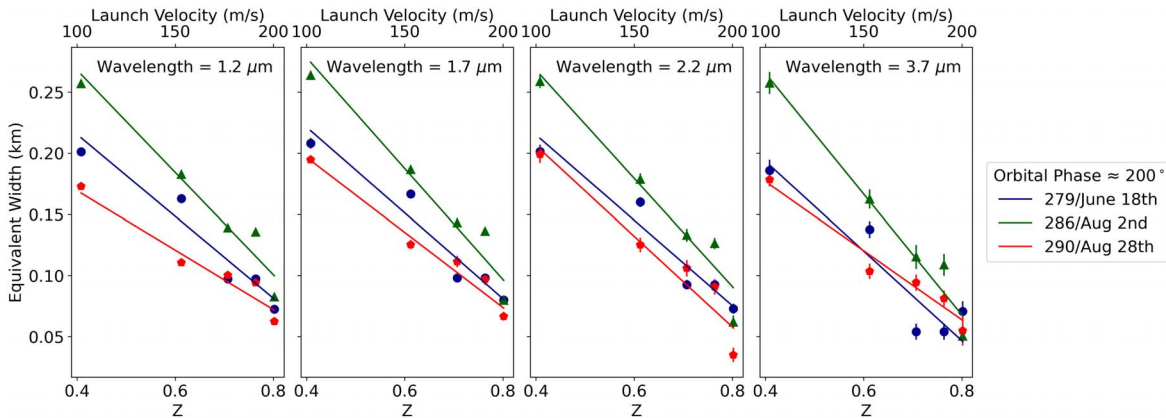

Figure 4. The integrated brightness of the plume (equivalent width) as a function of the parameter Z ($=[z/(r_E + z)]^{1/2}$, where $r_E = 250$ km is the radius of Enceladus and z is the plume's altitude) and launch velocity v (calculated using Equation (1)). The equivalent widths for the three different dates 2017 June 18, August 2, and August 28 are plotted (in blue, green, and red, respectively) at similar orbital phase value of $\simeq$200° and four different wavelengths. The equivalent width is fit to a linear function of Z. Note that the brightness of the plume is higher for the observation on August 2 (in green) than for the observations on the other dates.

signal-to-noise ratio in the spectra. Note that each of these sets of cubes corresponds to a relatively narrow range of orbital phases, so this averaging does not significantly affect our ability to quantify variations in plume activity. Table 1 shows the range of cubes corresponding to each orbit and the number of cubes before binning and after binning sets of 10 cubes each.

From each of these coadded cubes, we derive plume spectra as a function of altitude. Preliminary investigations of these data indicated that the majority of the plume signal exists between $x = -400$ and 400 km. Any signal in the range $x < -400$ km and $x > 400$ km is therefore primarily due to background signals from the instrument or the E ring. We

estimated this background by fitting the brightness values for -700 km $< x < -400$ km and $x > 400$ km at each value of y to a linear trend. Note that the brightness beyond $x < -700$ km is not included in this linear fit because this region appears to be more strongly contaminated by instrumental backgrounds than the rest of the reprojected image at certain wavelengths. After removing the background across all values of x, we define the plume's equivalent width at each y corresponding to an altitude z such that $z = -(250 + y)$ in km is the total integrated brightness in a horizontal slice through the plume (Hedman et al. 2013). The equivalent width is calculated as the sum of the signal across the x dimension multiplied by the step width
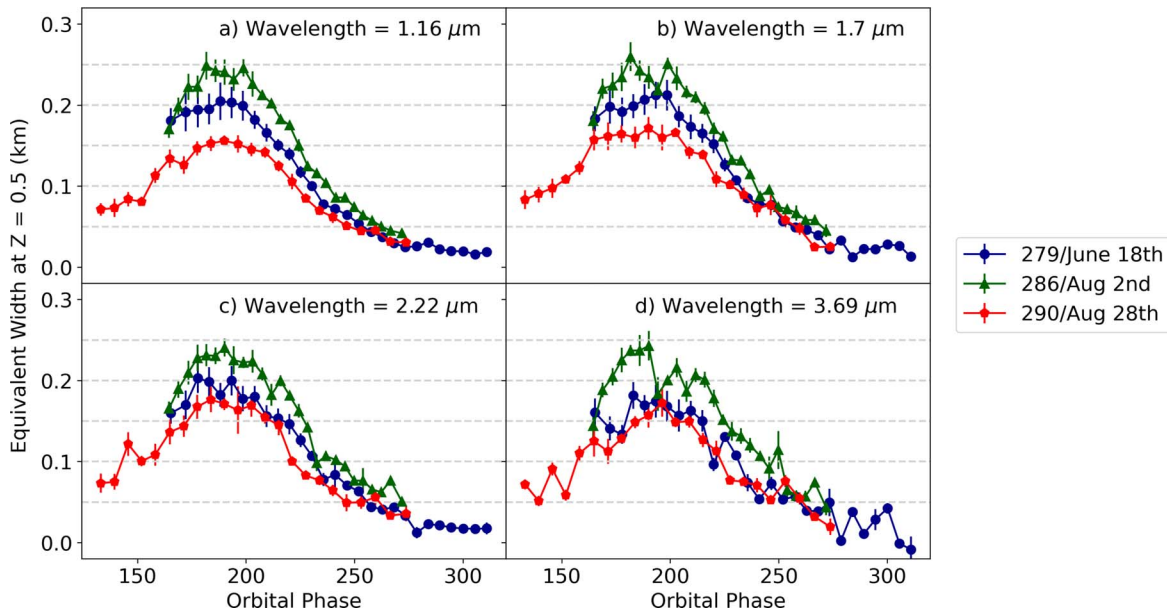
Figure 5. The plume's equivalent width at $Z = 0.5$ (altitude $z = 85$ km) as a function of orbital phase for the three dates and four different wavelength values. The plume's maximum brightness around the orbital phase of 180° is consistent at all wavelengths. Additionally, note that the brightness of the plume was higher on August 2 than it was on 2017 June 18 or August 28 at all wavelengths.

(that is, 100 km). This yields the plume's equivalent width for all y between -2000 and -300 km, or altitudes z ranging from 50 to 1750 km. This process is carried out on each binned cube for all wavelength channels of each of the three dates.

Figure 3 shows example plume spectra from 0.9 to 4.0 μm obtained from cubes obtained close to the peak of Enceladus's activity and at low altitudes. Each of these spectra has a clear dip around 3 μm corresponding to the fundamental water-ice absorption band (Mastrapa et al. 2009). While the signal-to-noise ratio of these spectra is reasonably good, for other orbital phases and altitudes it is still rather low, and so to better quantify relevant spectral trends, we further average these spectra over wavelength.

For this analysis we focus primarily on wavelength ranges outside the water-ice absorption band. Hence, we first apply a median filter to find outliers before 2.5 μm and after 3.3 μm. More specifically, we compute the median of the signal before 2.5 μm and flag outliers beyond the range of 1.5 times the standard deviation of all the points in this range, and then we do the same for the signals beyond 3.3 μm. This threshold value of 1.5σ was chosen because it was found to remove clear outliers based on visual inspection of selected spectra. After flagging these general outliers, we compute the average and error on the mean signal in bins of eight wavelength channels each. These averages and errors are computed after excluding both the outliers flagged previously and any data points that are beyond the 2σ range from the median of the eight wavelength channels that are being averaged together. This leaves us with 23 averaged wavelength values, which are shown as the connected lines in Figure 3. Finally, we compute the weighted average equivalent width over four wavelengths each and obtain the plume's output centered at 1.2, 1.7, 2.2, and 3.7 μm. This last averaging step improves the signal-to-noise ratio considerably and is particularly useful for the calculations of overall plume output and typical launch velocity described in the next subsection.

### 2.3. Quantifying Trends with Altitude and Orbital Phase/Time

In order to better quantify the trends in the brightness with time and altitude, we use the same basic parameterization as Hedman et al. (2013). That work defined a parameter $Z = [z/(r_E + z)]^{1/2}$, where $r_E = 250$ km is the radius of Enceladus and z is the plume's altitude. This parameter is useful because for low optical depth systems like the plume it is reasonable to assume that Enceladus's gravity is the dominant force acting on the particles and the particle density and gas density are so low that the particles follow purely ballistic trajectories. In this limit, the particle launch velocity v is directly related to the maximum altitude it reaches ($= z$):

$$v = v_{esc}\left[\frac{z}{r_E + z}\right]^{1/2} = v_{esc} * Z, \qquad (1)$$

where $v_{esc} = 240$ m s^{-1} is the escape velocity on Enceladus. Thus, for a population of particles, trends in the plume's brightness with Z reflect trends in the particles' launch velocity. Hedman et al. (2013) found that at wavelengths around 1 μm the relationship between equivalent width and Z was roughly linear with a negative slope.

Figure 4 shows that the approximately linear relationship between the plume's integrated brightness and the Z parameter observed by Hedman et al. (2013) also holds for the VIMS observations in 2017 over all the observed wavelengths. We therefore fit a linear trend to the plume's equivalent width profile versus Z in Figure 4 at altitudes between 50 and 450 km, i.e., Z between 0.41 and 0.8 and launch velocity v between 100 and 200 m s^{-1}.

The parameters for this linear fit are then used to calculate two quantities. One parameter is the equivalent width (a measure of the plume's total brightness) at a reference altitude of $z = 85$ km ($Z = 0.5$; $v = 120$ m s^{-1}) calculated through interpolation using the slope and the y-intercept, while the other is a critical velocity v_c, which is the value of v where the linear trend in the equivalent width would pass through zero.
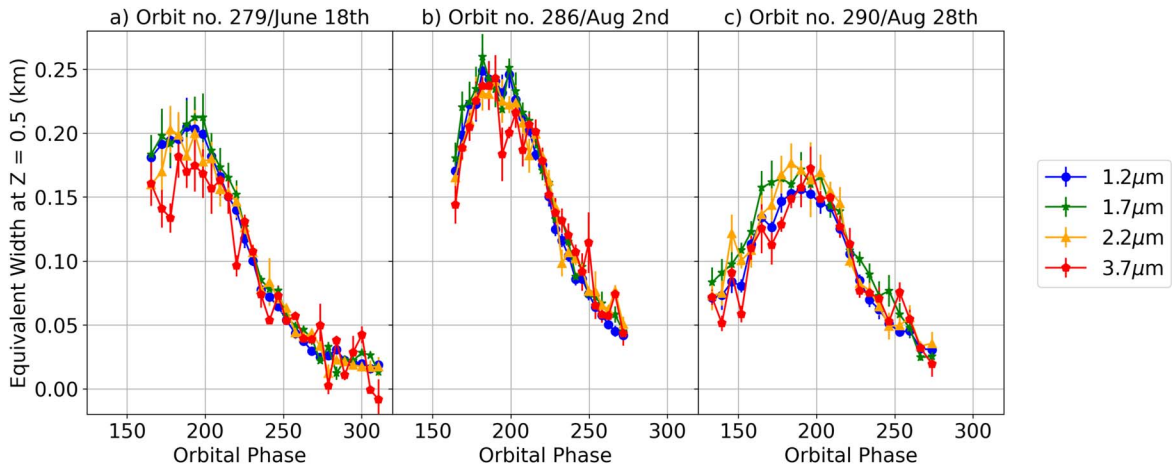
Figure 6. The plume's equivalent width at $Z = 0.5$ (altitude $z = 85$ km, same as Figure 5) as a function of orbital phase, grouped by the Orbit no./Date instead of wavelength. Note that on August 2 the brightness variations are nearly identical at all wavelengths; spectral trends in the plume's brightness can be seen in both the June 18 and August 28 data at orbital phases below 180°.
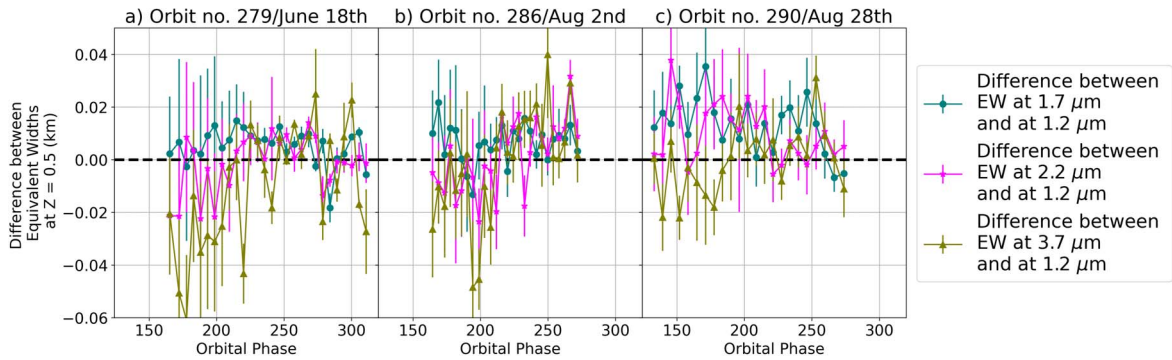
Figure 7. The difference in the plume's equivalent width at different wavelengths and at $Z = 0.5$ (altitude $z = 85$ km) as a function of orbital phase, grouped by the Orbit no./Date. Note that on August 2 the brightness variations are nearly identical at all wavelengths; spectral trends in the plume's brightness can be seen in both the June 18 and August 28 data at orbital phases below 180°.

Note that the critical velocity defined above involves an extrapolation of the linear fit into regions where it is not necessarily appropriate since this parameter often exceeds the escape velocity of Enceladus v_{esc}. Hence, we instead use this parameter to compute a quantity called the typical launch velocity $v_{typical}$. This corresponds to the weighted average of launch velocities of the particles visible between altitudes of 50 and 450 km:

$$v_{typical} = \frac{\int_{v_{min}}^{v_{max}} n(v)v\,dv}{\int_{v_{min}}^{v_{max}} n(v)\,dv}, \quad (2)$$

where $v_{min} = 100$ m s^{-1} and $v_{max} = 200$ m s^{-1} are the minimum and maximum launch velocities, respectively, of particles in the range of altitude 50–450 km, and $n(v)$ is the launch velocity distribution of the particles. For this analysis, we assume $n(v) \propto (1 - v/v_c)$, consistent with the observed linear trend between equivalent width and launch velocity shown in Figure 4. Using these values, Equation (2) can be reduced to

$$v_{typical} = \frac{\left[\frac{v_{max}^2}{2} - \frac{v_{max}^3}{3v_c}\right] - \left[\frac{v_{min}^2}{2} - \frac{v_{min}^3}{3v_c}\right]}{\left[v_{max} - \frac{v_{max}^2}{2v_c}\right] - \left[v_{min} - \frac{v_{min}^2}{2v_c}\right]}. \quad (3)$$

Using the above equations, the typical launch velocity is calculated for each binned cube. Since the trends among the different panels in Figure 4 are nearly the same, the typical launch velocity should not depend strongly on wavelength.

3. Results

Figures 5 and 6 show the plume's equivalent width at $Z = 0.5$ as a function of orbital phase for all three dates (June 18, August 2, and August 28) at four different wavelengths. In addition, Figure 7 shows the differences in the equivalent width at different wavelengths for each of the three dates. The equivalent width parameter provides an estimate of the plume's overall brightness and therefore the moon's overall activity level. All three observations covered the range of orbital phase 160°–270°. The plume's maximum brightness is consistently around the orbital phase of 180° for all these observations, regardless of wavelength. This confirms that the plume's ice-particle output is highest when the satellite is farthest from Saturn, consistent with prior analysis of ISS and VIMS plume observations (Hedman et al. 2013; Nimmo et al. 2014; Ingersoll & Ewald 2017; see also Figure 1).

Closer comparisons of these data with the ISS data reported in Ingersoll et al. (2020) not only confirm some of the variations documented in that work but also highlight novel spectral trends. In Figure 5 at wavelengths of 1.2 μm the trends
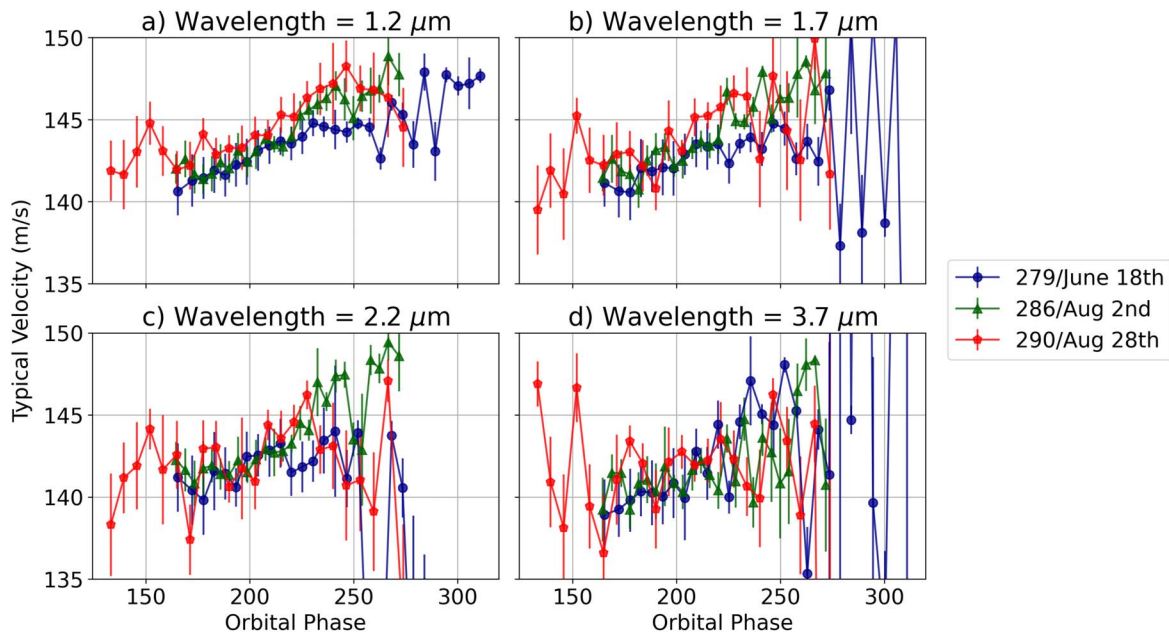
Figure 8. Typical launch velocity (in m s^{-1}) for three different orbits derived using Equation (3) as a function of orbital phase. Note that the typical launch velocity is higher on August 28 than on June 18 or August 2 at lower wavelengths of 1.2 μm. The typical launch velocity also generally increases with orbital phase. Note also that the variations in the typical launch velocity with wavelength are relatively small.

Table 2
Typical Launch Velocity for the Three Orbits Being Studied in This Paper across Orbital Phase and Wavelength

Wavelength (μm)	Orbital Phase (deg)	Typical Launch Velocity (m s^{-1})		
		279 Jun 18	286 Aug 2	290 Aug 28
0.95–1.37	174.6	141.3 ± 0.7	141.7 ± 0.5	142.9 ± 0.6
	196.0	142.4 ± 0.7	142.6 ± 0.5	143.5 ± 0.6
	217.4	143.7 ± 0.5	143.9 ± 0.3	145.1 ± 0.5
	238.4	144.5 ± 0.4	146.2 ± 0.4	147.5 ± 1.0
	260.2	144.8 ± 0.2	146.9 ± 0.5	146.8 ± 1.1
1.50–1.89	174.6	141.1 ± 0.8	141.4 ± 0.5	142.6 ± 0.8
	196.0	142.2 ± 0.7	142.7 ± 0.4	142.8 ± 0.6
	217.4	143.1 ± 0.7	144.2 ± 0.4	145.6 ± 0.5
	238.4	144.1 ± 0.3	146.5 ± 0.2	145.9 ± 1.3
	260.2	143.4 ± 0.6	148.1 ± 0.4	147.7 ± 1.5
2.01–2.41	174.6	140.7 ± 1.1	141.8 ± 0.6	141.9 ± 0.9
	196.0	141.7 ± 0.7	141.6 ± 0.5	140.8 ± 0.8
	217.4	142.3 ± 0.8	143.2 ± 0.3	145.0 ± 0.5
	238.4	142.2 ± 0.9	145.8 ± 0.4	142.7 ± 1.2
	260.2	142.6 ± 0.6	148.3 ± 0.5	145.5 ± 1.1
3.49–3.90	174.6	139.7 ± 0.9	140.7 ± 0.5	142.5 ± 0.7
	196.0	140.3 ± 1.0	140.8 ± 0.4	142.2 ± 0.9
	217.4	141.7 ± 0.6	141.9 ± 0.5	142.2 ± 0.7
	238.4	145.0 ± 0.5	142.0 ± 0.8	144.5 ± 0.8
	260.2	146.1 ± 0.3	148.2 ± 0.3	143.1 ± 1.4

with time and orbital phase among the observations are similar to those seen at visible wavelengths (Ingersoll et al. 2020), with the plume being brighter on August 2 than it was on June 18 and August 28, indicating that the overall activity level in the plume rose and fell during the 10-week interval of these observations. However, the relative brightness of the plume on June 18 and August 28 also varies with wavelength (see also Figures 6 and 7). At short wavelengths of 1.2 and 1.7 μm

shown in panels (a) and (b) of Figure 5, the plume is significantly brighter on June 18 (in blue) than it was on August 28 (in red), which is consistent with prior analysis of the imaging data (Ingersoll et al. 2020). However, at a longer wavelength of 3.7 μm in panel (d) of Figure 5, the plume's brightnesses on these two dates (in blue and red) are nearly identical. See Section 4 for further details on this variation.

Figure 8 shows the typical launch velocity of the plume particles derived from the same linear fits described above as a function of orbital phase for the same four average wavelength values and three observation dates. The typical launch velocities plotted across orbital phase in Figure 8 are averaged using the inverse of variance as weights. The weighted averages of these typical launch velocities across four wavelength ranges and five orbital phase values are also provided in Table 2. Unlike the dramatic variations seen in the plume's brightness, this parameter depends much less on orbital phase, date, or wavelength. In general, the typical launch velocity increases with increasing orbital phase between 160° and 230°. The spectral variations in the typical launch velocity are subtle, with the values at 3.7 μm being only about 10 m s^{-1} less than the values at 1.2 μm (see Table 2). This is consistent with Figure 4, where the linear trends for each Orbit no./Date are similar for all the different wavelengths. Also note that at 1.2 μm the typical launch velocity is slightly higher on August 28 than on June 18 or August 2.

4. Discussion

Figures 5–7 show several interesting trends with orbital phase, time, and particularly wavelength. Since the wavelength trends are the most unique aspect of these new VIMS data, we will focus primarily on these aspects of the data here. In general, particles of different sizes scatter different wavelengths of light with different efficiencies, so the spectral trends provide information about trends with particle size. Detailed modeling of these spectra will be the subject of a future work,

but we can already highlight some interesting trends with wavelength that likely reflect trends with particle size. VIMS data are observed at high phase angles, where particles scatter light most efficiently at wavelength comparable to the particle radius (Van de Hulst 1957; Hedman et al. 2009). Hence, larger particles contribute more to the plume's brightness at longer wavelengths. In other words, larger particles tend to produce a spectrum with a redder slope.

Variations in the plume spectra indicative of variations in the particle size distribution are most easily seen in Figure 7. On June 18, the olive green curve is more negative (brightness decreases from 1.7 to 3.7 μm), hinting at a higher number of small particles in the plume on that date. While on August 28 both the magenta and teal curves are above the zero line (brightness increases from 1.2 to 1.7 and 2.2 μm). This variation is also visible in the spectra shown in Figure 3, where the August 28 data show a redder slope than the earlier data on June 18 and August 2. This indicates that the plume contained a higher fraction of larger particles on August 28 than on June 18.

These changes in the plume's spectra may provide additional clues about what happened to produce the brightness changes across these three dates. One potential explanation for these changes is that they reflect localized sources turning on and off. Individual jets have been observed to turn on and off over timescales that are not explicable by simple tidal models (Porco et al. 2014; Spitale et al. 2017, 2020; Ingersoll et al. 2020). The maximum in plume brightness might be due to a highly collimated jet only seen on August 2 (Ingersoll et al. 2020). However, this change in plume activity could also be explained by subsequent opening of new channels or choking of conduits by ice deposition on the surface near the channels (Ingersoll & Pankine 2010; Spencer et al. 2018). Changes in the particle size distribution as a whole from one month to another could shed light on the cause of this stochastic variability in the plume, such as how these variations reflect changes in vent conditions. We plan to further explore the particle size variations in the plume using Mie scattering in our future work.

Figure 8 shows that for all three orbits the typical launch velocity of particles increases with orbital phase after the satellite passes the plume maxima near apocenter. This increase in the velocity with orbital phase holds true for all wavelengths and is consistent with prior results (Hedman et al. 2013; Ingersoll et al. 2020). This suggests an inverse relation between the particle mass flux and ejection velocity at least in the region beyond apoapsis. Another key observation is that the typical launch velocity is higher on August 28 than on June 18 and August 2 at wavelengths of 1.2 μm, while the particle mass flux reflected by the equivalent width in Figure 5 is lowest. This further alludes to a complementary change in particle mass flux and typical launch velocity at least at 1.2 μm. One possible explanation for this is the narrowing of vents due to changing tidal stresses; as the satellite crosses its apocenter the flow speed might increase while the mass flux decreases (but see Nimmo et al. 2014, for potential complications with this idea).

Interestingly, the launch velocity of particles in Table 2 and Figure 8 shows only a slight decrease as wavelength increases. This is surprising because previously published models by Schmidt et al. (2008) predict substantial variations of launch velocity with particle size. According to these models, repeated collisions with the walls of the conduit reduce the particle velocity relative to the gas. Degruyter & Manga (2011) also

modeled the particle acceleration within the conduit and their ballistic transport once they exited the vent using the gas flow model of Ingersoll & Pankine (2010) and the Schmidt et al. (2008) collision model and similarly found that larger particles achieve lower exit speeds. Using the Schmidt et al. (2008) collision model for a gas density of 4.85 g m^{-3}, a gas speed of 500 m s^{-1}, and a collision length of 0.1 m, a large fractional reduction of 0.98 is expected in the typical particle velocity as size increases from 1.2 to 3.7 μm. By contrast, the typical launch velocities in Figure 8 show a fractional reduction of only 0.01–0.16 as wavelength increases from 1.2 to 3.7 μm, which is 6 times lower than predicted by previous models of particle velocities. While the plume's brightness at a given wavelength is due to particles with a range of sizes, this is still a notable difference.

This finding is also consistent with some of the earlier spectral analysis of the Enceladus plume. Hedman et al. (2009) determined the relative number of particles of radii 1, 2, and 3 μm versus height in early VIMS plume observations, which were in turn converted into velocity distribution of particles. Data obtained at orbital phases around 90°–120° indicated that the number density of larger particles of radius 3 μm falls faster than the smaller particles of radius 1 μm, implying a typical lower launch velocity for 3 μm particles, which was roughly consistent with Schmidt et al. (2008). However, the velocity distribution for the data obtained closest to apoapsis (shown in Figure 6 of that paper) is not significantly steeper for larger particle sizes, indicating that the typical launch velocity of larger particles does not decrease steeply, which is more consistent with these observations.

One possible explanation for this surprisingly subtle reduction in particle velocity with increasing particle size is that the vent parameters are different from what was assumed in the Schmidt et al. (2008) model. Changing these parameters such that the critical grain radius is larger could result in a less steep dependence of ejection velocity on grain sizes in the range from submicrons to a few microns (Postberg et al. 2009, 2011; Schmidt 2014). Another possible explanation is that particle–particle interactions at the vent are more common than previously thought. Unlike collisions with the walls of the conduit (which produce trends in particle velocity with size; Schmidt et al. 2008), particle–particle collisions would cause grains of different sizes to have similar velocity distributions. Both particle–wall and particle–particle collisions are most important near the vent, where the gas density rapidly declines, and the particles become partially decoupled from the gas (so that they are launched at much lower velocities than the gas; Goldstein et al. 2018). Assuming a gas density and a particle density of 10^{23} m^{-3} and 2.1×10^{10} m^{-3}, respectively (Yeoh et al. 2017), at the end of the conduit, the mean free path for particle–gas collision is of the order of 10^{-13} m, while for particle–particle collision it is 1 m. The mean free path for particle–particle collisions is comparable to the measured vent sizes on the south pole of Enceladus. Goguen et al. (2013) estimated a fissure width of 9 m based on near-IR thermal emission spectra acquired by VIMS, and Yeoh et al. (2015) estimated vent diameters of up to 2.8 m. Hence, particle–particle interactions could occur at a high enough rate to affect particle velocities, which has not been taken into account in the current models.

We plan to model the observed spectral trends to obtain quantitative constraints on the particle size distribution at

different altitudes and times. This information should further information about conditions within the vents.

Acknowledgments

Appendix
Cubes Excluded from Analysis

The following cubes were removed from the data on June 18/ Orbit no. 279: CM_1876443559_1, CM_1876443614_1, CM_1876443669_1, CM_1876443724_1, CM_1876445164_1, CM_1876446029_1, CM_1876446202_1, CM_1876446375_1, CM_1876457449_1, CM_1876470103_1, CM_1876474082_1, CM_1876488640_1, CM_1876493658_1, CM_1876493831_1, CM_1876494004_1, CM_1876494177_1, CM_1876494350_1, CM_1876494523_1, CM_1876494696_1, CM_1876494869_1, CM_1876495042_1, CM_1876495215_1.

The following cubes are removed during background removal from the data on August 2/Orbit no. 286: CM_1880355922_1, CM_1880358137_1, CM_1880366306_1, CM_1880369490_1, CM_1880380704_1, CM_1880390533_6, CM_1880391952_6, CM_1880392472_6, CM_1880392610_6, CM_1880392818_6, CM_1880392852_6, CM_1880393025_6, CM_1880393233_6, CM_1880393337_6, CM_1880393441_6, CM_1880393579_6, CM_1880393718_1, CM_1880394687_6, CM_1880394791_6, CM_1880395102_6, CM_1880395241_6, CM_1880395794_6, CM_1880395967_6, CM_1880396071_6.

The following cubes are removed during background removal from the data on August 28/Orbit no. 290: CM_1882608048_5, CM_1882637326_1, CM_1882640856_1, CM_1882644178_1, CM_1882644386_1, CM_1882645009_1, CM_1882646047_1, CM_1882646255_1, CM_1882646463_1, CM_1882646670_1, CM_1882646878_5.

ORCID iDs

H. Sharma ⬤ https://orcid.org/0000-0002-0803-2678
M. M. Hedman ⬤ https://orcid.org/0000-0002-8592-0812

References

Brilliantov, N. V., Schmidt, J., & Spahn, F. 2008, P&SS, 56, 1596
Brown, R. H., Baines, K. H., Bellucci, G., et al. 2004, SSRv, 115, 111
Clark, R. N., Brown, R. H., Lytle, D. M., & Hedman, M. 2018, The VIMS Wavelength and Radiometric Calibration 19, Final Report, NASA Planetary Data System
Degruyter, W., & Manga, M. 2011, GeoRL, 38, L16201
Dougherty, M., Khurana, K., Neubauer, F., et al. 2006, Sci, 311, 1406
Ermakov, A. I., Park, R. S., Roa, J., et al. 2021, PSJ, 2, 157
Goguen, J. D., Buratti, B. J., Brown, R. H., et al. 2013, Icar, 226, 1128
Goldstein, D. B., Hedman, M., Manga, M., et al. 2018, in Enceladus and the Icy Moons of Saturn, ed. P. M. Schenk et al. (Tucson, AZ: Univ. Arizona Press), 175
Hansen, C. J., Esposito, L., Stewart, A., et al. 2006, Sci, 311, 1422
Hedman, M., Gosmeyer, C., Nicholson, P., et al. 2013, Natur, 500, 182
Hedman, M., Nicholson, P., Showalter, M., et al. 2009, ApJ, 693, 1749
Helfenstein, P., & Porco, C. C. 2015, AJ, 150, 96
Hurford, T. A., Helfenstein, P., Hoppa, G. V., Greenberg, R., & Bills, B. G. 2007, Natur, 447, 292
Hurford, T. A., Helfenstein, P., & Spitale, J. N. 2012, Icar, 220, 896
Ingersoll, A. P., & Ewald, S. P. 2017, Icar, 282, 260
Ingersoll, A. P., Ewald, S. P., & Trumbo, S. K. 2020, Icar, 344, 113345
Ingersoll, A. P., & Pankine, A. A. 2010, Icar, 206, 594
Kieffer, S. W., Lu, X., Bethke, C. M., et al. 2006, Sci, 314, 1764
Kite, E. S., & Rubin, A. M. 2016, PNAS, 113, 3972
Mastrapa, R. M., Sandford, S. A., Roush, T. L., Cruikshank, D. P., & Dalle Ore, C. M. 2009, ApJ, 701, 1347
Nakajima, M., & Ingersoll, A. P. 2016, Icar, 272, 309
Nimmo, F., Porco, C., & Mitchell, C. 2014, AJ, 148, 46
Nimmo, F., Spencer, J., Pappalardo, R., & Mullen, M. 2007, Natur, 447, 289
Porco, C., DiNino, D., & Nimmo, F. 2014, AJ, 148, 45
Porco, C., Mitchell, C., Nimmo, F., & Tiscareno, M. 2018, LPSC, 49, 2003
Porco, C. C., Helfenstein, P., Thomas, P., et al. 2006, Sci, 311, 1393
Postberg, F., Kempf, S., Schmidt, J., et al. 2009, Natur, 459, 1098
Postberg, F., Schmidt, J., Hillier, J., Kempf, S., & Srama, R. 2011, Natur, 474, 620
Schenk, P. M., Clark, R. N., Howett, C. J., Verbiscer, A. J., & Waite, J. H. 2018, in Enceladus and the Icy Moons of Saturn, ed. P. M. Schenk et al. (Tucson, AZ: Univ. Arizona Press)
Schmidt, J. 2014, AGUFM, P51F–05
Schmidt, J., Brilliantov, N., Spahn, F., & Kempf, S. 2008, Natur, 451, 685
Smith-Konter, B., & Pappalardo, R. T. 2008, Icar, 198, 435
Spahn, F., Schmidt, J., Albers, N., et al. 2006, Sci, 311, 1416
Spencer, J., Nimmo, F., Ingersoll, A. P., et al. 2018, in Enceladus and the Icy Moons of Saturn, ed. P. M. Schenk et al. (Tucson, AZ: Univ. Arizona Press), 163
Spencer, J., Pearl, J., Segura, M., et al. 2006, Sci, 311, 1401
Spitale, J., Tigges, M., Rhoden, A., Hurford, T., & Webster, K. 2020, AAS/ DPS Meeting Abstracts, 52, 215.05
Spitale, J. N., Hurford, T., & Rhoden, A. R. 2017, AAS/DPS Meeting, 49, 207.02
Spitale, J. N., & Porco, C. C. 2007, Natur, 449, 695
Teolis, B. D., Perry, M. E., Hansen, C. J., et al. 2017, AsBio, 17, 926
Van de Hulst, H. 1957, Light Scattering by Small Particles (New York: Wiley)
Waite, J. H., Jr., Combi, M. R., Ip, W.-H., et al. 2006, Sci, 311, 1419
Waite, J. H., Jr., Lewis, W., Magee, B., et al. 2009, Natur, 460, 487
Yeoh, S. K., Chapman, T. A., Goldstein, D. B., Varghese, P. L., & Trafton, L. M. 2015, Icar, 253, 205
Yeoh, S. K., Li, Z., Goldstein, D. B., et al. 2017, Icar, 281, 357